Accepted Manuscript

A solution to transient seepage in unsaturated porous media

Dorival M. Pedroso

PII: S0045-7825(14)00488-5
DOI: http://dx.doi.org/10.1016/j.cma.2014.12.009
Reference: CMA 10504

To appear in: *Comput. Methods Appl. Mech. Engrg.*

Received date: 8 July 2014
Revised date: 2 December 2014
Accepted date: 4 December 2014

Please cite this article as: D.M. Pedroso, A solution to transient seepage in unsaturated porous media, *Comput. Methods Appl. Mech. Engrg.* (2014), http://dx.doi.org/10.1016/j.cma.2014.12.009

A solution to transient seepage in unsaturated porous media

Dorival M. Pedroso[a,*]

[a]*School of Civil Engineering, The University of Queensland, St Lucia QLD 4072, Australia*

Abstract

This paper presents a solution to seepage problems in porous media considering the complete time-dependent transition from fully saturation to partially unsaturated states and *vice-versa*; therefore capturing the evolution of the free surface (region with zero liquid pressure). A simple and efficient method to implement the seepage face boundary condition for finite element solutions is proposed. The method is based on an analogy to unilateral constraints in Plasticity and, in essence, adds some extra unknowns to the finite elements with boundaries near the seepage face. The free surface is thus automatically predicted. The resulting enriched elements can also account for ponding or infiltration at the external surface. The solution is accomplished by considering the theory of porous media with slightly compressible liquids. The formulation can easily accommodate liquid retention models with hysteresis. Verification examples are presented in addition to simulations of drainage and infiltration illustrating the capabilities of the proposed solution.

Keywords:
Transient analysis, unilateral boundary conditions, free surface, infiltration, ponding, unsaturated soils

1. Introduction

Seepage problems are an important topic in engineering and have particular applications to groundwater simulations or geotechnical engineering. For

*Corresponding author
Email address: d.pedroso@uq.edu.au (Dorival M. Pedroso)

instance, it is common practice to import data from seepage analyses into stability codes for risk assessment of slopes and retaining walls. Analytical solutions are available for simple situations [1, 2] and geometric configurations and numerical methods are usually employed to the more complex cases.

Among the numerical methods for seepage analyses, the finite element is perhaps the mostly used in the industry and by researchers [3]. One major difficulty for analytical or numerical solutions is the representation of the unilateral constraints at the seepage face. To circumvent this problem, a number of strategies has been proposed in the literature and some include iterative techniques while others use mesh adaptivity [4–7]. The topic is still active with some recent papers published [8–12].

The modelling of fluid flow in unsaturated soils can be consistently derived from the theory of porous media (TPM) [13]. The TPM is a continuum mechanics approach in which a macroscopic formulation is obtained for each constituent in addition to the whole mixture. This theory has its origins on the concept of volume fractions and the theory of mixtures and has been improved along the years resulting in a rational methodology to represent the complex behaviour of porous media in a simple way [14].

One important aspect to be considered when modelling unsaturated porous media is the so-called water retention curve (or liquid retention model – LRM) [15–21]. This curve represents the link between liquid saturation and capillary pressure hence closing the system of equations in addition to introducing each particular material behaviour into the computational model. One common observed characteristics of the LRM is the hysteresis and scanning curves that appear during experiments with cycles of drainage and imbibition. These may cause difficulties in the numerical analyses; however the presented formulation can easily accommodate hysteretic models [22].

This paper is organised as follows. In section 2, a brief review of the theory of porous media is presented with focus on deriving the governing equation for seepage analyses. In section 3, the treatment of unilateral constraints for the seepage face and corresponding solution with enriched elements are proposed. In section 4, constitutive models for the liquid retention behaviour and the liquid conductivity are introduced. In section 5, some verification simulations are discussed and the predictive capabilities are illustrated. Finally, the conclusions are given in section 6.

In this paper, the order of a tensor variable is indicated by the number of dots added under the corresponding symbol – *underdot* as diacritic marks in phonetics. For instance, $\underset{\cdot}{\boldsymbol{a}}$ and $\underset{\cdot\cdot}{\boldsymbol{a}}$ are (different) tensors of first and second

orders, respectively – confusion is avoided because of the underdots. Inner products are expressed with operator dots such as in $s = \underset{.}{\boldsymbol{a}} \cdot \underset{.}{\boldsymbol{a}}$ and $\sigma = \underset{..}{\boldsymbol{a}} : \underset{..}{\boldsymbol{a}}$. The dyadic product is expressed as $\underset{..}{\boldsymbol{a}} = \underset{.}{\boldsymbol{a}} \otimes \underset{.}{\boldsymbol{a}}$.

2. Governing equations and numerical solution

The governing equations are derived with basis on the theory of porous media (TPM). The solution is then obtained with the finite element method [3, 23, 24]. Further details, especially on the derivation of all equations for porous media, are found in the works by de Boer, Ehlers, Lewis, Schrefler and Pedroso [13, 14, 25, 22].

2.1. Governing equations

In the TPM, each material constituent $\alpha := \{s, \ell, g\}$ (solid, liquid, gas) in a representative elementary volume (REV) is characterised by its volume fraction n_α which is then used to define a partial density quantity ρ_α by means of weighting the real density ρ^α. For the fluid constituents $\beta := \{\ell, g\}$, it is also convenient to define the saturation s_β and pressure p_β. Another useful quantity is the volume fraction of fluids n_f which is equal to the porosity when all pores are interconnected. These key quantities are summarised in Eq. (1)

$$n_\alpha = \frac{dv_\alpha}{dv} \qquad \rho_\alpha = n_\alpha \, \rho^\alpha \qquad s_\beta = \frac{dv_\beta}{dv_v} \qquad n_f = \frac{dv_v}{dv} \tag{1}$$

where dv is the volume of the REV, dv_α the volume of each particular constituent, and dv_v the volume of all fluid constituents in the REV; for instance, with liquids and gases: $dv_v = dv_\ell + dv_g$. We also define the partial density of the mixture ρ by adding the three partial densities. For a three-constituents system, ρ and other easily verifiable expressions can be written as follows

$$\rho = \rho_\ell + \rho_s + \rho_g \qquad n_f = n_\ell + n_g \qquad n_\ell + n_g + n_s = 1 \qquad \rho_\beta = n_f \, s_\beta \, \rho^\beta \tag{2}$$

An important concept required to close the system of equations is the liquid retention model. With the following definition of capillary pressure

$$p_c = p_g - p_\ell \tag{3}$$

the liquid retention model can be expressed by

$$C_c = \frac{\mathrm{d}s_\ell}{\mathrm{d}p_c} \tag{4}$$

For the following derivations – and the whole extent of this paper, the gas phase is disregarded with the pressure on the gas being assumed equal to zero; thus $p_g = 0$, $\dot{p}_g = 0$ and $p_c = -p_\ell$.

The flow of fluids within the porous medium is best expressed in terms of an Eulerian framework in which the solid skeleton serves as reference. For the seepage modelling, the solid matrix is considered to be perfectly rigid and the seepage velocity of liquid $\dot{\boldsymbol{w}}_\ell$ is introduced. The relative velocity $\dot{\boldsymbol{w}}_\ell$ allows for the definition of a viscous interaction term and the interaction term $\hat{\dot{\boldsymbol{p}}}_\ell$ in the balance of linear momentum [14]. With basis on the dissipation inequality, the following simple form that can recover Darcy's model for steady saturated flow is assumed [14, 25]

$$\hat{\dot{\boldsymbol{p}}}_\ell = \frac{\partial n_\ell}{\partial \dot{\boldsymbol{x}}}\, p_\ell - \frac{n_\ell^2\, g\, \rho^\ell}{k_\ell^r}\, (\ddot{\boldsymbol{k}}_\ell^{sat})^{-1} \cdot \dot{\boldsymbol{w}}_\ell \tag{5}$$

where g is the gravity acceleration, k_ℓ^r is a multiplier that depends on the liquid saturation, and $\ddot{\boldsymbol{k}}_\ell^{sat}$ is a tensor analogous to the Darcy's conductivity parameter (with components given in m/s for example).

Now, based on the above definitions, the following governing equations are obtained by invoking the balances of mass and linear momentum of liquid; see e.g. [25]

$$\begin{aligned} &\text{bal. of mass of liquid:} && C_{p\ell}\, \dot{p}_\ell + \operatorname{div}(\rho_\ell\, \dot{\boldsymbol{w}}_\ell) = 0 \\ &\text{bal. of lin. momentum of liquid:} && \rho_\ell\, \dot{\boldsymbol{w}}_\ell = k_\ell^r\, \ddot{\boldsymbol{K}}_\ell^{sat} \cdot (\rho^\ell\, \boldsymbol{g} - \nabla\, p_\ell) \end{aligned} \tag{6}$$

where $\ddot{\boldsymbol{K}}_\ell^{sat} = \frac{\ddot{\boldsymbol{k}}_\ell^{sat}}{g}$ and the following nonlinear coefficient $C_{p\ell}(p_\ell, s_\ell)$ is defined

$$C_{p\ell} = n_f\, \left(s_\ell\, C_\ell - \rho^\ell\, C_c\right) \tag{7}$$

with $C_\ell = \frac{\partial \rho^\ell}{\partial p_\ell}$ expressing the compressibility model for the liquid constituent. In this paper, a large value for C_ℓ is adopted in order to simulate a nearly incompressible liquid. Note that $C_{p\ell}$ is just the total derivative of ρ_ℓ with respect to p_ℓ, i.e.

$$C_{p\ell} = \frac{\mathrm{d}\rho_\ell}{\mathrm{d}p_\ell} = \frac{\cancel{\mathrm{d}n_f}}{\cancel{\mathrm{d}p_\ell}}\, s_\ell\, \rho^\ell + n_f\, \underbrace{\frac{\mathrm{d}s_\ell}{\mathrm{d}p_\ell}}_{-C_c}\, \rho^\ell + n_f\, s_\ell\, \underbrace{\frac{\mathrm{d}\rho^\ell}{\mathrm{d}p_\ell}}_{C_\ell} \tag{8}$$

It can be seen that Eq. (6)b reduces to Darcy's model for steady flows. Besides, Eq. (6)b can be substituted into Eq. (6)a resulting in a diffusion equation.

2.2. Finite element solution

The numerical solution of the transient seepage problem is achieved by first approximating time with the θ-method. Afterwards, space is approximated by the standard Bubnov-Galerkin finite element method [3, 23]. It is observed that this order (time first, space later) yields great convenience when dealing with complex liquid retention models (e.g. with hysteresis) [22]. As shown in the following, the Newton-Raphson method can then be directly applied after deducing the derivatives related with the liquid retention model.

By employing the θ-method from time step ${}^{n}t$ to the time step ${}^{n+1}t$, the following approximated rate is obtained

$$ {}^{n+1}\dot{p}_\ell \approx \beta_1 \, {}^{n+1}p_\ell - \psi_\ell^* \tag{9} $$

where the auxiliary variable ψ_ℓ^* is function of the solution variable at time $t = {}^{n}t$ only; i.e. it is known at the beginning of the time increment. This variable can be computed by means of:

$$ \psi_\ell^* = \beta_1 \, p_\ell^n + \beta_2 \, \dot{p}_\ell^n \tag{10} $$

where the β_k coefficients are function of the θ_k parameters that define the method and are given by

$$ \beta_1 = \frac{1}{\theta \, h} \quad \text{and} \quad \beta_2 = \frac{1 - \theta}{\theta} \tag{11} $$

Note that this form does not allow for explicit solutions with $\theta = 0$. Unconditionally stability is obtained with $\theta \geq \frac{1}{2}$. In this work, $\theta = \frac{1}{2}$ is chosen.

The time approximation of the balance equations is obtained by substituting ${}^{n+1}\dot{p}_\ell$ into Eq. (6), resulting in

$$ r_\ell \equiv \underbrace{C_{p\ell} \, (\beta_1 \, p_\ell - \psi_\ell^*)}_{\bar{r}_\ell} + \operatorname{div} (\rho_\ell \, \boldsymbol{w}_\ell) \tag{12} $$

where r_ℓ is an auxiliary variable and the expression for $\rho_\ell \, \boldsymbol{w}_\ell$ defined in Eq. (6)b is implicitly considered for the sake of convenience. Moreover, all variables in the above equation are defined at the updated time $n + 1$; although the superscripts were dropped. Therefore, the solution is *implicit* and iterations are required.

To proceed, the solution domain is indicated by Ω and its boundary by Γ. The boundary is divided into regions where either essential or natural

conditions are specified. The following boundary conditions and regions are considered

$$\begin{aligned} \text{pressure specified:} \quad & p_\ell = \bar{p}_\ell \quad && \text{on} \quad \Gamma_p \\ \text{flux specified:} \quad & \dot{\boldsymbol{w}}_\ell \cdot \hat{\dot{\boldsymbol{n}}} = \bar{q}_\ell \quad && \text{on} \quad \Gamma_q \\ \text{mixed:} \quad & f\, g = 0 \quad && \text{on} \quad \Gamma_f \end{aligned} \tag{13}$$

where $\Gamma = \Gamma_p \cup \Gamma_q \cup \Gamma_f$ and $\Gamma_p \cap \Gamma_q = \Gamma_q \cap \Gamma_f = \emptyset$ define some restrictions on the division of boundary regions. The mixed boundary condition is discussed below.

The collections of trial solutions $\mathcal{S}$ and weighting functions $\mathcal{V}$ are defined next. They are sets of H^1 functions and are denoted in compact form according to

$$\mathcal{S}_p = \{p_\ell : \Omega \to \mathbb{R} \,|\, p_\ell \in H^1,\, p_\ell = \bar{p}_\ell \;\text{ on }\; \Gamma_p\} \tag{14}$$

The weak form of Eq. (12) (in the updated time increment) is finally obtained after multiplying Eq. (12) by an arbitrary weight η and integrating it over the volume Ω of the domain under study. By also considering the Green-Gauss (divergence) theorem, the procedure results in

$$\int_\Omega \eta\, \bar{r}_\ell \,\mathrm{d}\Omega + \int_\Gamma \eta\, \rho_\ell\, \bar{q}_\ell \,\mathrm{d}\Gamma - \int_\Omega \nabla \eta \cdot (\rho_\ell\, \dot{\boldsymbol{w}}_\ell) \,\mathrm{d}\Omega \tag{15}$$

where Γ indicates the boundary of the domain with specified flux $\bar{q}_\ell \equiv \dot{\boldsymbol{w}}_\ell \cdot \hat{\dot{\boldsymbol{n}}}$ in which $\hat{\dot{\boldsymbol{n}}}(\dot{\boldsymbol{x}})$ is the unit vector normal at the boundary (surface).

It is worth noting that, upon the application of the divergence theorem, the variable ρ_ℓ is left out of the specified flux term $\bar{q}_\ell$ because, in this way, the seepage velocity at the boundary can be directly specified – not the weighted seepage (or filter) velocity $\rho_\ell\, \dot{\boldsymbol{w}}_\ell$ as done in other papers. Moreover, ρ_ℓ depends on saturation according to Eq. (2)d and the saturation at the boundary is not known *a priori*. Therefore, because saturation depends on pressure, the derivative of the surface boundary condition term with respect to pressure is also required during the solution of this nonlinear problem. The details are given as follows.

A set of approximation spaces are chosen to the primary variable (p_ℓ) and the weights (η), as standard in finite elements [3]. The approximation of p_ℓ is

$$p_\ell^m(\dot{\boldsymbol{x}}) \approx \sum_m S^m(\dot{\boldsymbol{\xi}}(\dot{\boldsymbol{x}}))\, p_\ell^m \tag{16}$$

where $S^m(\boldsymbol{\xi})$ are the interpolation (shape) functions, defined over the parent space with natural coordinates $\boldsymbol{\xi}(\boldsymbol{x})$. The gradient of the shape function corresponding to node m is symbolised by $\boldsymbol{G}^m(\boldsymbol{\xi})$. Thus, the resulting space discretised form is

$$R_\ell^m = \int_{\Omega_e} S^m \, \bar{r}_\ell \, \mathrm{d}\Omega + \int_{\Gamma_e} S_\Gamma^m \, \rho_\ell \, \bar{q}_\ell \, \mathrm{d}\Gamma - \int_{\Omega_e} \boldsymbol{G}^m \cdot (\rho_\ell \, \boldsymbol{w}_\ell) \, \mathrm{d}\Omega \tag{17}$$

where the boundary conditions are yet to be specified. Note that the *assembly* of the above equations has to be applied with the integrations being performed over the domain of the element Ω_e or its boundary Γ_e. Note also that the weights vanish at the boundaries with essential conditions prescribed; see mentioned references for further details and, in particular, [3].

Three types of boundary conditions are considered: (1) pressure specified; (2) flux specified; and (3) a mix of both defining an unilateral constraint. The last one leads to the so-called seepage face condition and is explained in details in the next section.

The solution of Eq. (17) is briefly discussed as well. Newton's method is employed in order to find a set of nodal values p_ℓ^m that makes all the m residuals R_ℓ^m to reduce towards zero. An error measure and corresponding tolerance is then selected. For a given time increment Δt, a number of iterations are carried out if the first trial R_ℓ^m is not zero (within a tolerance). During each iteration, the derivative of R_ℓ^m with respect to p_ℓ^n is required; this can be computed as follows

$$\frac{\mathrm{d}R_\ell^m}{\mathrm{d}p_\ell^n} = \int_{\Omega_e} S^m \frac{\mathrm{d}\bar{r}_\ell}{\mathrm{d}p_\ell^n} \, \mathrm{d}\Omega + \int_{\Gamma_e} S_\Gamma^m \frac{\mathrm{d}\rho_\ell}{\mathrm{d}p_\ell^n} \, \bar{q}_\ell \, \mathrm{d}\Gamma - \int_{\Omega_e} \boldsymbol{G}^m \cdot \frac{\mathrm{d}(\rho_\ell \, \boldsymbol{w}_\ell)}{\mathrm{d}p_\ell^n} \, \mathrm{d}\Omega \tag{18}$$

where $\frac{\mathrm{d}R_\ell^m}{\mathrm{d}p_\ell^n}$ can be assembled into to the Jacobian matrix. These expressions are given in Appendix A. Nonetheless, the calculation of $\frac{\mathrm{d}\rho_\ell}{\mathrm{d}p_\ell^n}$ at the integration points on the surface of the element requires a special treatment and is discussed as follows. Actually, the presence of ρ_ℓ in Eq. (17) makes the system much more complicated than the corresponding one for fully liquid saturated media. Note that the saturation values are computed at the integration points of the finite element and ρ_ℓ needs to be computed at the boundary. Thus, the strategy developed here is to first extrapolate $\rho_\ell(\boldsymbol{\xi}_k) = n_f \, s_\ell \, \rho^\ell$ from the integration points (k) to the nodes (m) of the solid element and second to interpolate the nodal values ρ_ℓ^m to the integration points $(\boldsymbol{\xi}^*)$ at

the surface of the element. Mathematically, this is expressed as follows

$$\rho_\ell^m \approx \sum_k^{N_{ip}} E_k^m \, \rho_\ell(\boldsymbol{\xi}_k) \tag{19}$$

where E_k^m is an extrapolation array (*extrapolator*) with a shape defined by the number of nodes (N_n) and the number of integration points (N_{ip}). If the number of integration points is equal to the number of nodes, the extrapolator E_k^m can be directly computed from the inversion of a matrix built with the shape functions. However, this cannot be easily done if those numbers are different. Another strategy is to employ least squares but the results may lead to oscillations. A better method to compute E_k^m was proposed in [26] and is therefore employed in the present work. The interested reader is kindly directed to the cited paper for further details.

After the extrapolation is performed and ρ_ℓ^m are obtained, $\rho_\ell(\boldsymbol{\xi}^*)$ corresponding to the integration points $\boldsymbol{\xi}^*$ at the surface of the element are calculated by means of conventional interpolation as follows

$$\rho_\ell(\boldsymbol{\xi}^*) \approx \sum_m^{N_{nf}} S_\Gamma^m(\boldsymbol{\xi}^*) \, \rho_\ell^m \tag{20}$$

where N_{nf} indicates the number of nodes at a particular face of the element. The derivative of $\rho_\ell(\boldsymbol{\xi}^*)$ required in Eq. (18) can then be computed by means of

$$\left.\frac{\mathrm{d}\rho_\ell}{\mathrm{d}p_\ell^n}\right|_{\boldsymbol{\xi}^*} = \sum_m S_\Gamma^m \sum_k E_k^m \left.\frac{\mathrm{d}\rho_\ell}{\mathrm{d}p_\ell^n}\right|_{\boldsymbol{\xi}_k} \tag{21}$$

or, by recalling Eq. (8),

$$\left.\frac{\mathrm{d}\rho_\ell}{\mathrm{d}p_\ell^n}\right|_{\boldsymbol{\xi}^*} = \sum_m S_\Gamma^m \sum_k E_k^m \, C_{p\ell}(\boldsymbol{\xi}_k) \, S^n(\boldsymbol{\xi}_k) \tag{22}$$

The resulting expression can be easily implemented in a finite element code alongside the other derivatives in Eq. (18). In this way, the convergence of the nonlinear solver is quadratic. For the presented numerical simulations, the quadratic convergence is observed.

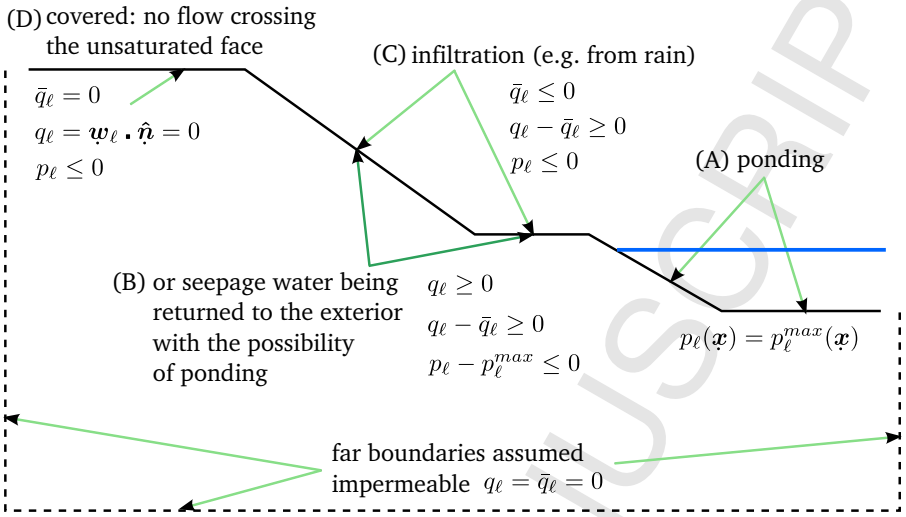

Figure 1: Complex boundary conditions at the surface of a porous domain. Example of a sloped land with groundwater and rain.

3. Modelling the transient seepage face

The modelling of the conditions at the surface of an unsaturated porous domain involves the specification of unilateral boundary conditions (Fig. 1); see the excellent discussion in [27, 10]. The situation is even more complex when these conditions change over time. To illustrate, suppose the sloped land exemplified in Fig. 1 is initially flooded up to the middle bench and then rain starts raising the water level to the upper bench. During this period, the boundary conditions change from flux prescribed at parts of the surface to $p_\ell(\boldsymbol{x}) = p_\ell^{max}(\boldsymbol{x})$ entirely.

In Fig. 1, $q_\ell(\boldsymbol{x}) = \boldsymbol{w}_\ell \cdot \hat{\boldsymbol{n}}$ is the actual seepage velocity at the surface whereas $\bar{q}_\ell(t)$ is the prescribed one. The difference $q_\ell - \bar{q}_\ell$ is always positive or zero. If $\bar{q}_\ell > 0$, water is being removed from the system and, in this case, $q_\ell = \bar{q}_\ell$. On the other hand, under rain or irrigation with $\bar{q}_\ell < 0$, water may infiltrate or escape through the seepage face but the difference is also greater than zero. For instance, when infiltration occurs, $q_\ell < 0$ and $|q_\ell| < |\bar{q}_\ell|$ resulting in $q_\ell - \bar{q}_\ell > 0$. When leakage occurs, $q_\ell > 0$ yielding also $q_\ell - \bar{q}_\ell > 0$ since $-\bar{q}_\ell$ is a positive quantity.

The situation of prescribed pressure or ponding at the surface can be expressed by means of $p_\ell - p_\ell^{max} \leq 0$, with p_ℓ^{max} being the prescribed value or the maximum expected/allowed pressure. Therefore, the conditions along

the whole surface in Fig. 1, including the three benches (continuous lines) can uniquely be described by means of

$$\underbrace{q_\ell(t,\dot{\boldsymbol{x}}) - \bar{q}_\ell(t)}_{f(t,\dot{\boldsymbol{x}})} \geq 0, \tag{23}$$

$$\underbrace{p_\ell(t,\dot{\boldsymbol{x}}) - p_\ell^{max}(t,\dot{\boldsymbol{x}})}_{g(t,\dot{\boldsymbol{x}})} \leq 0 \tag{24}$$

and

$$f(t,\dot{\boldsymbol{x}})\, g(t,\dot{\boldsymbol{x}}) = 0 \tag{25}$$

where the "flux" function f and the "gap" function g (term borrowed from [27]) are both function of space and time. Note that the condition above is analogous to the *complementarity conditions* for the yield function and plastic multiplier in Plasticity; see e.g. [28], and hence, one equivalent approach developed for plastic models in [29] is taken into consideration. In this approach, Eqs. (23), (24) and (25) are replaced by

$$r_f = f - \langle f + \kappa\, g \rangle \tag{26}$$

where κ is a coefficient to ensure dimensional consistency and $\langle x \rangle$ is the ramp function (Macaulay brackets) defined as follows

$$\langle x \rangle = \begin{cases} 0 & \text{if } x < 0 \\ x & \text{otherwise} \end{cases} \tag{27}$$

Fig. 2 illustrates Eq. (26) where it may be seen that the function is discontinuous at $r_f(0,0)$ and that the solution $r_f = 0$ represents either $g \leq 0$ or $f \geq 0$ as required; thus satisfying Eqs. (23), (24) and (25).

Due to the discontinuity, it is convenient to replace the Macaulay brackets with a smooth approximation $\langle\langle x \rangle\rangle$. The approximation in [29] is chosen to do so and is written as

$$\langle\langle x \rangle\rangle = x + \tfrac{1}{\beta} \log\left[1 + \exp\left(-\beta\, x\right)\right] \tag{28}$$

where β is a large number. The use of $\langle\langle x \rangle\rangle$ in r_f is illustrated in Fig. 3.

Now, for the finite element solution, f can be viewed as an unknown. Therefore, we propose to enrich the finite element with f_ℓ^μ primary variables in which μ corresponds to the nodes at the exterior faces of the element

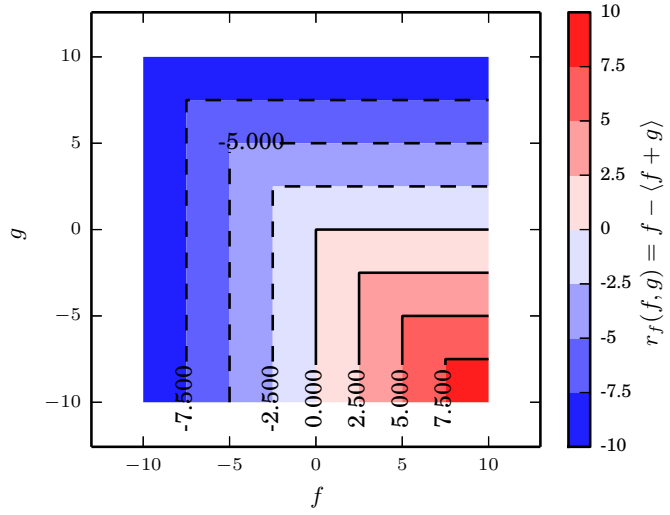

Figure 2: Use of ramp function to define the constraints conditions.

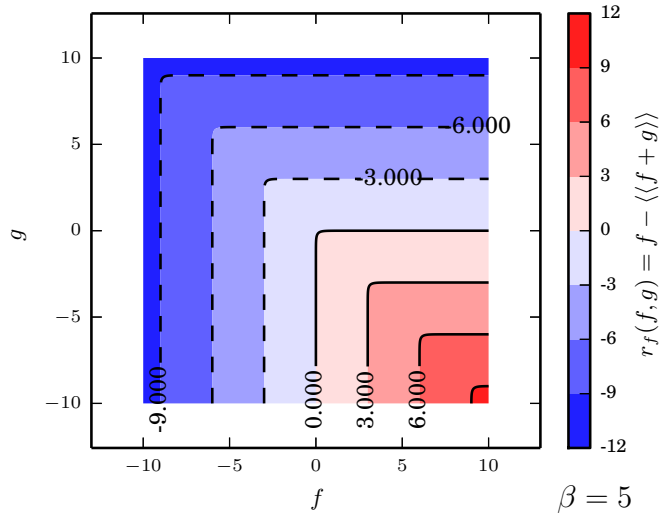

Figure 3: Use of a smoothed function to define the constraints conditions ($\beta = 5$).

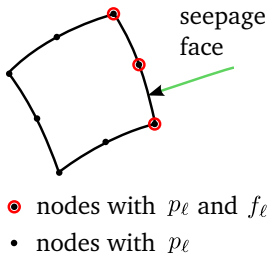

Figure 4: Enriched element with additional primary variables.

where infiltration or seepage is expected (Fig. 4). In a sense, the "degrees of freedom" (DOF) f_ℓ^μ act as Lagrangian multipliers. With isoparametric elements, $f_\ell(\boldsymbol{x})$ along the surface are approximated as follows (see Eq. 20)

$$f_\ell(\boldsymbol{\xi}^*) \approx \sum_{\mu}^{N_{nf}} S_\Gamma^\mu(\boldsymbol{\xi}^*)\, f_\ell^\mu \tag{29}$$

and an extra term is added to Eq. (17) [10, 27]

$$R_x^m = \int_{\Gamma_e} S_\Gamma^m \underbrace{\rho_\ell \langle\langle f_\ell + \kappa\, g \rangle\rangle}_{r_x} \,\mathrm{d}\Gamma \tag{30}$$

The solution is achieved by also minimising r_f in Eq. (26). Therefore, the following equation is introduced

$$R_f^\mu = \int_{\Gamma_e} S_\Gamma^\mu\, r_f \,\mathrm{d}\Gamma \tag{31}$$

Note that R_f^μ weakly satisfies the constraints expressed by Eq. (26) and is required to close the system of equations due to the extra unknowns f_ℓ^μ. The effect of Eq. (30) is explained as follows:

- If $g = 0$, p_ℓ is fully specified and $\langle\langle f_\ell + \kappa\, g \rangle\rangle = \langle\langle f_\ell \rangle\rangle$ adds an outward flux to enforce the prescribed p_ℓ^{max} value (case A in Fig. 1).
- If $f_\ell = 0$, flux is prescribed by $\bar{q}_\ell$ and $\langle\langle f_\ell + \kappa\, g \rangle\rangle = \langle\langle \kappa\, g \rangle\rangle$ adds an extra outward flux to enforce $\kappa\, g \leq 0$ thus modelling the seepage boundary with an atmospheric condition or an allowed ponding (case B in Fig. 1).
- If $f_\ell > 0$, $\kappa\, g = 0$ and $\langle\langle f_\ell + \kappa\, g \rangle\rangle = \langle\langle f_\ell \rangle\rangle$ corresponds to the outward flux at the seepage face (case C in Fig. 1).

- If $\kappa\, g < 0$, $f_\ell = 0$ and $\langle\langle f_\ell + \kappa\, g\rangle\rangle = \langle\langle \kappa\, g\rangle\rangle = 0$; thus, the boundary is impermeable (case A in Fig. 1).

The derivatives of Eq. (31) are also required when using Newton's method to solve the nonlinear problem – as in this paper. These derivatives are given in Appendix Appendix A for the sake of completeness. The Jacobian matrix for Newton's method will then have the following form

$$\begin{bmatrix} \frac{\mathrm{d}R_\ell^m}{\mathrm{d}p_\ell^n} & \frac{\mathrm{d}R_\ell^m}{\mathrm{d}f_\ell^\nu} \\ \frac{\mathrm{d}R_f^\mu}{\mathrm{d}p_\ell^n} & \frac{\mathrm{d}R_f^\mu}{\mathrm{d}f_\ell^\nu} \end{bmatrix} \tag{32}$$

4. Constitutive models

Two constitutive models are presented in this section: one for the liquid retention behaviour and another for the relationship between hydraulic conductivity and liquid saturation. Both are based on the concept of references introduced in [30]. The liquid retention model is well explained in [19, 20] and only a brief introduction is given here. The model for the hydraulic conductivity is discussed in this paper from the concept of references. Its main characteristics is to enforce a smooth transition between saturated and unsaturated regimes.

4.1. Liquid retention model

The rate-type model proposed in [19], which may or not include hysteresis, is considered in this paper. The model is illustrated in Figure 5 where two horizontal lines are selected as references, one passing through $s_\ell = 1$ and another through $s_\ell = y_r$. Another semi-vertical line with slope λ_d serves also as reference. This last one allows the definition of the reference curve $y_d(x)$ deduced by employing the distance D_d. Afterwards, the main curve is hierarchically defined by means of the distance D from the main curve to the reference curve $y_d(x)$. We note that, in this way, the calibration of parameters is quite simple requiring only geometric constructions. Note also that although residual saturation values y_r close to zero can be experimentally observed at times, for the numerical simulations, a minimum positive value is chosen instead since this value cannot be zero.

The main retention behaviour can now be expressed by means of

$$\frac{\mathrm{d}y}{\mathrm{d}x} = -\bar{\lambda}(x, y) \tag{33}$$

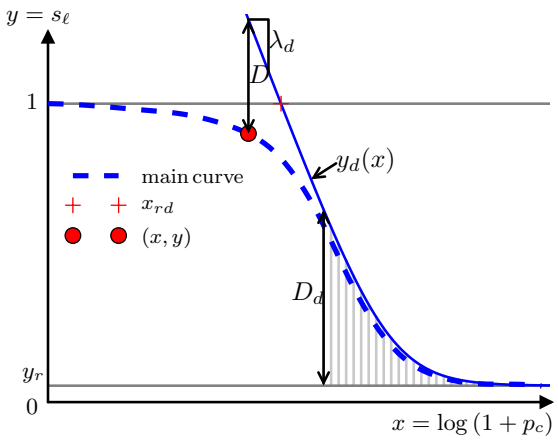

Figure 5: Liquid retention model based on the concept of references.

where the slope $\bar{\lambda}$ is computed with the equations in Tab. 1. Further discussions and detailed derivations are found in [19]. The solution of this expression can be obtained as in Computational Plasticity. In the present paper, an implicit backward Euler method is employed [22].

4.2. Liquid conductivity model

A common modelling approach for the dependence of hydraulic conductivity on saturation is to define a multiplier $0 \leq k_\ell^r(s_\ell) \leq 1$ (see Eq. 5). A versatile yet accurate model for k_ℓ^r can be obtained with the concept of references as illustrated in Figure 6. The model employs the equations introduced in [30] with a distance that decreases from right to left in the $k_\ell^r - s_\ell$ plane. The point $(s_\ell = 1, k_\ell^r = 1)$ is hence enforced while the value $k_\ell^r = \alpha_\ell$ is just approximated but being nearly exact with high values of the β_ℓ parameter. The slopes $\lambda_{0\ell}$ and $\lambda_{1\ell}$ can be easily calibrated by fitting experimental data. The model function and derivative are

$$k_\ell^r(s_\ell) = \lambda_{0\ell}\, s_\ell - \frac{1}{\beta_\ell} \log\left(c_3 + c_2\, e^{c_1\, s_\ell}\right) \tag{34}$$

and

$$\frac{\mathrm{d}k_\ell^r}{\mathrm{d}s_\ell} = \lambda_{0\ell} - \frac{c_1\, c_2\, e^{c_1\, s_\ell}}{\beta_\ell\, \left(c_3 + c_2\, e^{c_1\, s_\ell}\right)} \tag{35}$$

with

$$c_1 = \beta_\ell\, (\lambda_{0\ell} - \lambda_{1\ell}) \qquad c_2 = e^{-\beta_\ell\, \alpha_\ell} \qquad c_3 = e^{\beta_\ell\, (\lambda_{0\ell} - 1)} - c_2\, e^{c_1} \tag{36}$$

Table 1: Liquid retention model (see Fig. 5).

model
$D_d = \max(y - y_r, 0)$
$\bar{\lambda}_d = (1 - \mathrm{e}^{-\beta_d D_d})\,\lambda_d$
$y_d = -\lambda_d\, x + \frac{1}{\beta_d} \log(c_3^d + c_2^d\, \mathrm{e}^{c_1^d\, x})$
$D = \max(y_d - y, 0)$
$\bar{\lambda} = \bar{\lambda}_d\, \mathrm{e}^{-\beta_2\, D}$
constants
$c_1^d = \beta_d\, \lambda_d$
$c_2^d = \mathrm{e}^{\beta_d\, y_r}$
$c_3^d = \mathrm{e}^{\beta_d\,(1+\lambda_d\, x_{rd})} - c_2^d\, \mathrm{e}^{c_1^d\, x_{rd}}$

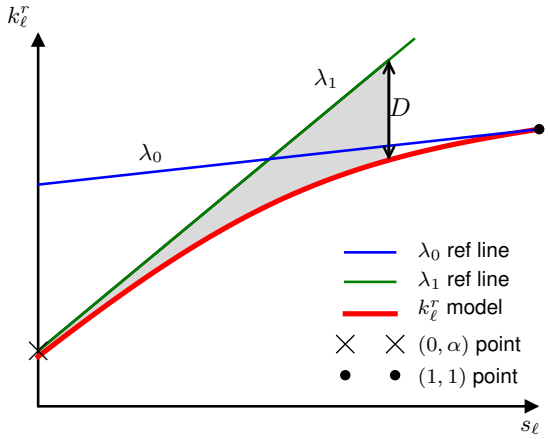

Figure 6: Liquid conductivity model based on the concept of references.

Table 2: Liquid isotropic conductivity and parameters for retention models.

Example	k_ℓ^{sat} [m/s]	λ_d	x_{rd}	y_r	β_d	β_2	Figure
1 2	1	3	0.6	0.005	3	3	8
3	Soil 1: $3 \cdot 10^{-9}$, Soil 2: 10^{-4}, Soil 3: 10^{-5}	3	3.0	0.005	2	2	9
4 5 6	1	3	2.0	0.005	2	2	10

5. Numerical simulations

Three verification problems and three illustrative simulations are presented in this section. Each verification problem has been thoroughly investigated by other authors and reference results are available for comparisons [5, 6, 8, 12]. While the reference results are obtained using iterations or mesh adaptations, our results are a direct outcome from the proposed transient formulation including the mixed boundary condition. For comparison purposes, the liquid retention models for the verification problems are calibrated in such a way to model as close as possible a discrete transition from saturated to unsaturated states. Note that the other methods assume a discrete model.

For all simulations, the properties of the porous medium and liquid (water) are $n_\ell = 0.3$, $\rho^\ell = 1\,\mathrm{Mg/m^3}$ and $K_\ell = 2.2 \cdot 10^6\,\mathrm{kPa}$. The parameters for the hydraulic conductivity model for all analyses are: $\lambda_{0\ell} = 0.001$, $\lambda_{1\ell} = 1.2$, $\alpha_\ell = 0.01$ and $\beta_\ell = 10$ (Fig. 7). The conductivity tensor is assumed isotropic and therefore k_ℓ^{sat} symbolises its repeated eigenvalues. The material parameters for the liquid retention models are given in Tab. 2 and the corresponding curves are illustrated in Figs. 8, 9 and 10.

Finally, the *datum* for computing the hydraulic head is located at $y = 0$ or $z = 0$ coordinate and the β coefficient in Eq. (28) is adopted equal to 70 for all simulations.

5.1. Example 1: Rectangular porous domain

This example is illustrated in Fig. 11. The full transient process is simulated from $t = 0$ to $t = 1000$ s with $\Delta t = 1$. The steady state is reached in the end. Since it is easier to dry the unsaturated domain instead of forcing wetting and also because only the steady solution is needed for the verification, the simulation is carried out by lowering the liquid level at the right-hand face from 10 m to 2 m linearly.

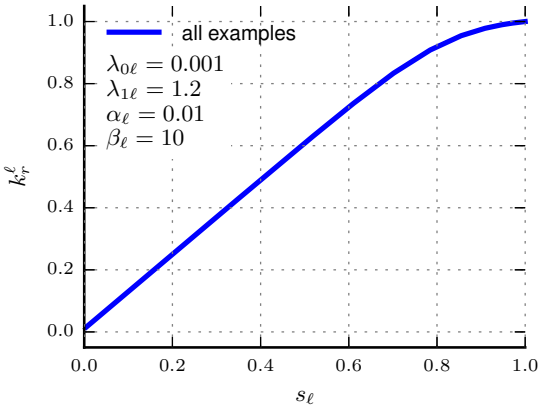

Figure 7: Liquid conductivity model for all examples.

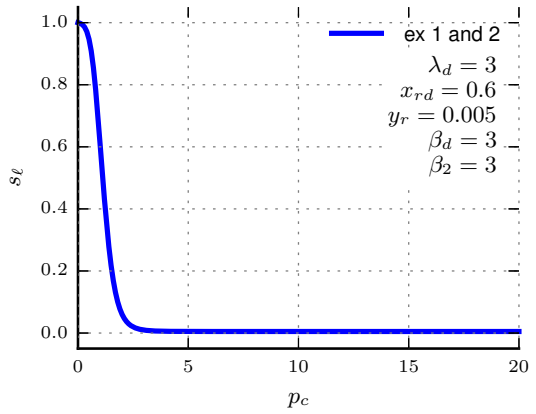

Figure 8: Liquid retention model for examples 1 and 2.

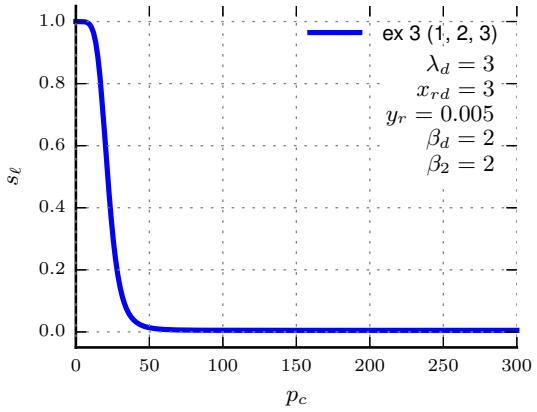

Figure 9: Liquid retention model for example 3.

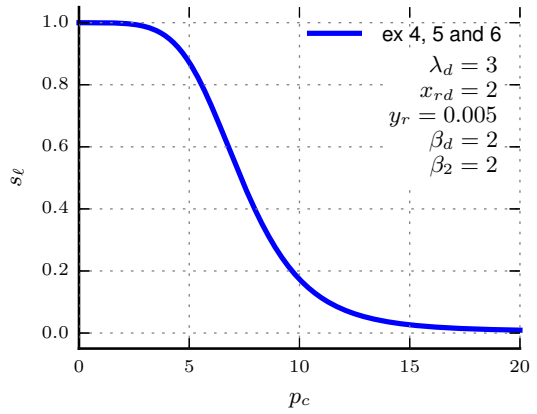

Figure 10: Liquid retention model for examples 4, 5 and 5.

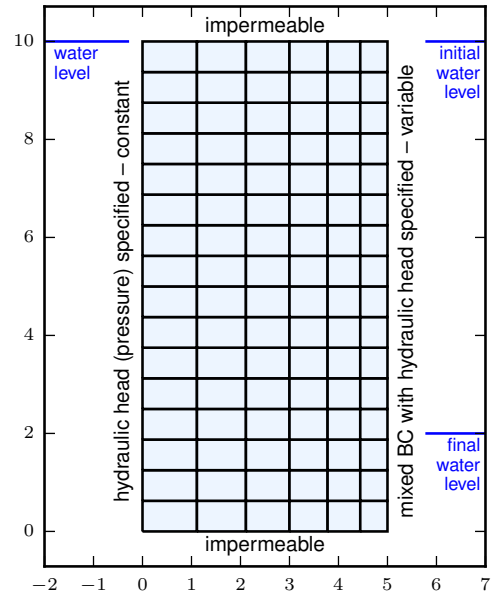

Figure 11: Example 1: Rectangular porous domain. Geometry, mesh and boundary conditions. The liquid level at the right-hand side is lowered to the indicated final position; thus the whole boundary is a seepage face. A zero liquid pressure defining the maximum "ponding" pressure is selected; i.e. $p_\ell^{max} = 0$. Mesh with 8-node quadrilaterals and 9 integration points.

The results for the final time output are presented in Fig. 12. It can be observed that the resulting free surface/phreatic line (region with zero liquid pressure) is comparable to other solutions [5, 6, 8, 12]. Note that by varying the water level at the right-hand face, the whole face is subjected to the unilateral conditions. Therefore, this example demonstrates the importance of the proper modelling of the seepage face in the transient process.

5.2. Example 2: Trapezoidal porous domain

This example is shown in Fig. 13 and performs a verification similar to Example 1. The simulation is again carried out by lowering the liquid level at the right-hand face of a sloped block. The resulting free surface is illustrated in Fig. 14 which is very similar to other reference solutions [5, 6, 8, 12].

To further illustrate the capabilities of the enriched elements and their ability to model the free surface crossing one side with mixed boundary condition, a two-element mesh is employed for this example (Fig. 15a). In

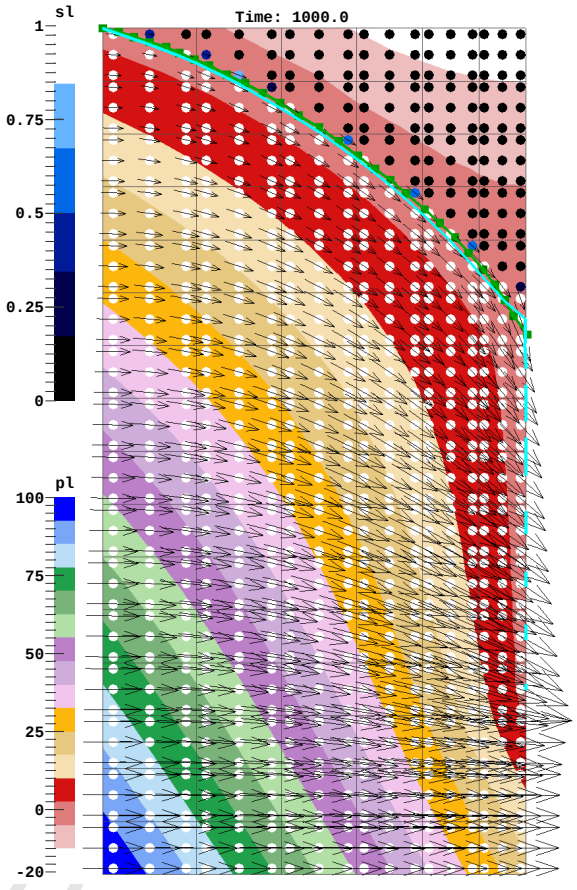

Figure 12: Example 1: Rectangular porous domain. The calculated phreatic line ($p_\ell = 0$) is indicated by a light blue line. The reference line from [12] is indicated in green with square markers. The circles indicate the saturation s_ℓ and the arrows the partial relative velocity $\rho_\ell \dot{\boldsymbol{w}}_\ell$ ($\times 0.5$) at the integration points.

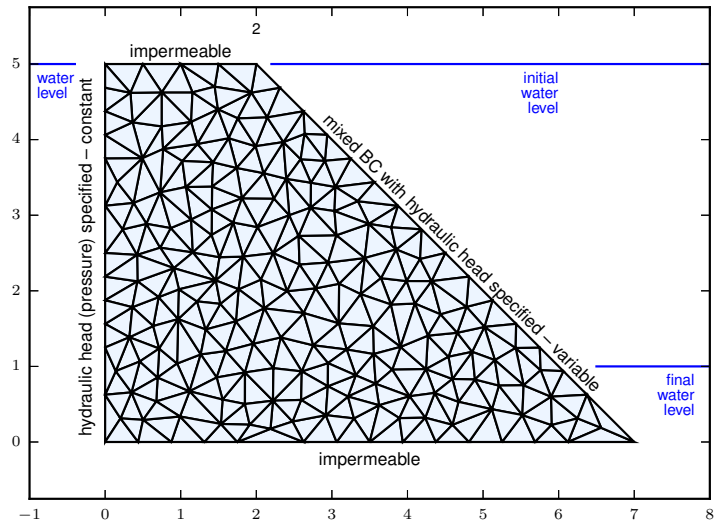

Figure 13: Example 2: Trapezoidal porous domain. Geometry, mesh and boundary conditions. The liquid level at the right-hand side is lowered as in Example 1. Mesh with 6-node triangles and 3 integration points.

addition, a mesh with quadrilaterals is used for comparison (Fig. 15b). The results are presented in Fig. 16 and show that the evolution of the phreatic line crossing the boundary can be modelled by one single element at the seepage face. Moreover, the phreatic lines at the end of the transient solution with the three meshes are not too different from the reference steady-state solution.

5.3. Example 3: Embankment dam

The next verification example models the seepage through a large dam with a very low permeability clay core. The mesh and boundary conditions are illustrated in Figs. 17 and 18. There are three regions with three materials as indicated by (1), (2), and (3) in the figure. The material parameters are presented in Tab. 2. This problem was analysed in [5]; the results from [9] are employed for comparisons.

As in the previous examples, the hydraulic head at the right-hand side of the dam is linearly reduced from 188 m to 142 m. The simulation is run from $t = 0$ to $t = 10^{-7}$ with $\Delta t = 10^3$; thus corresponding to a slow drawdown process.

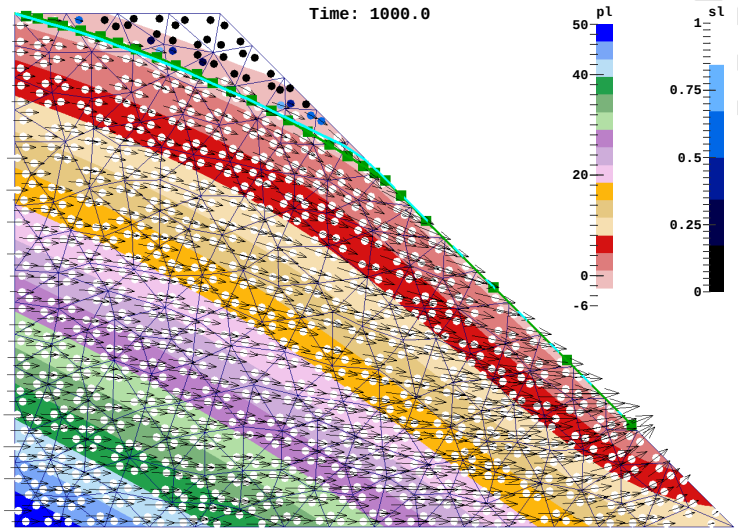

Figure 14: Example 2: Trapezoidal porous domain. The calculated phreatic line is indicated by a light blue line. The reference phreatic line from [12] is shown in green with square markers. Circles indicate liquid saturation. Arrows indicate partial relative velocity ($\times 0.5$).

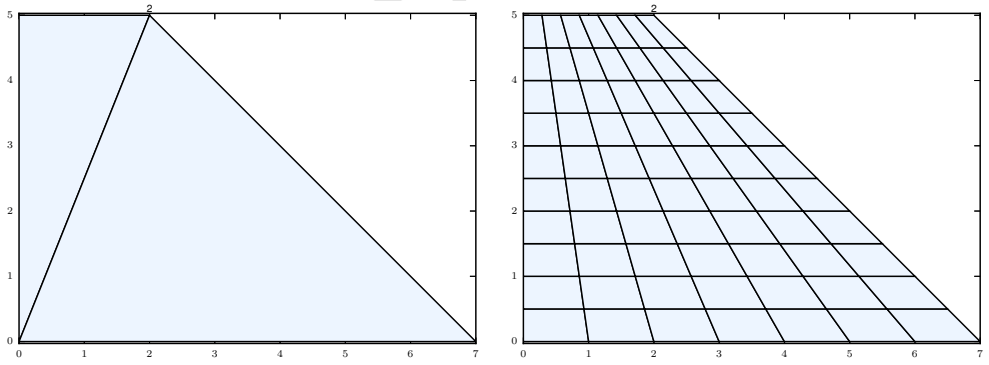

(a) (b)

Figure 15: Example 2: Trapezoidal porous domain. (a) coarser mesh with 6-node triangles and 3 integration points. (b) mesh with 8-node quadrilaterals and 9 integration points.

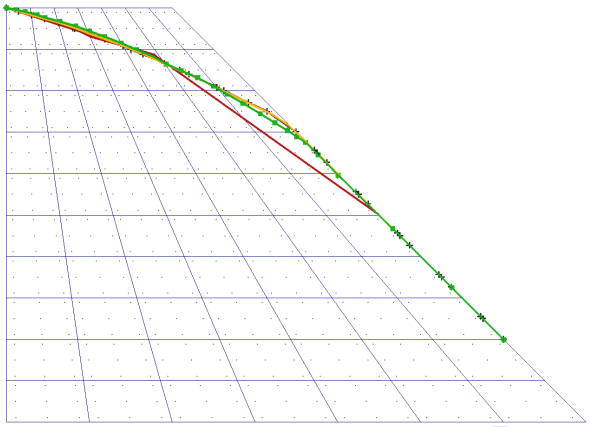

Figure 16: Example 2: Trapezoidal porous domain. The green line with square markers corresponds to the reference solution [12]. The black line with crosses and the yellow line correspond to the quad8 and tri6 meshes, respectively. The red line a little off the other lines corresponds to the two-element mesh.

The results from a number of times are given in Figs. 19, 20, 21 and 22. The partial relative velocity $\rho_\ell \boldsymbol{w}_\ell$ is illustrated with black arrows indicating the change on liquid velocity. The solution in [9] is highlighted in green while the solution by this paper is highlighted in light blue. We can observe that the final phreatic line matches fairly well the reference one, even though the liquid retention model is not as discrete as in the reference work. Nonetheless, our solution gives the complete history from saturated to unsaturated states.

5.4. Example 4: Wetting of unsaturated rectangular porous domain

To further illustrate the capabilities of the proposed model, a simulation starting with a dry material and ending with a wet one is carried out. This case is similar to a reverse simulation of Example 1. The mesh and boundary conditions are illustrated in Fig. 23 where the domain is initially unsaturated up to 2 m height and the liquid level at the left-hand side is slowly raised with the hydraulic head at the right-hand side being kept at 2 m. In this way, the dried material is subjected to wetting and the simulation is usually more challenging due to the smaller hydraulic conductivity of the dry material; see typical behaviour in Fig. 6.

The simulation is run from $t = 0$ to $t = 2000$ with $\Delta t = 1$. The results are given in Fig. 24 where it can be observed that the pressure-saturation distribution at the end is similar to the distribution obtained in Example 1.

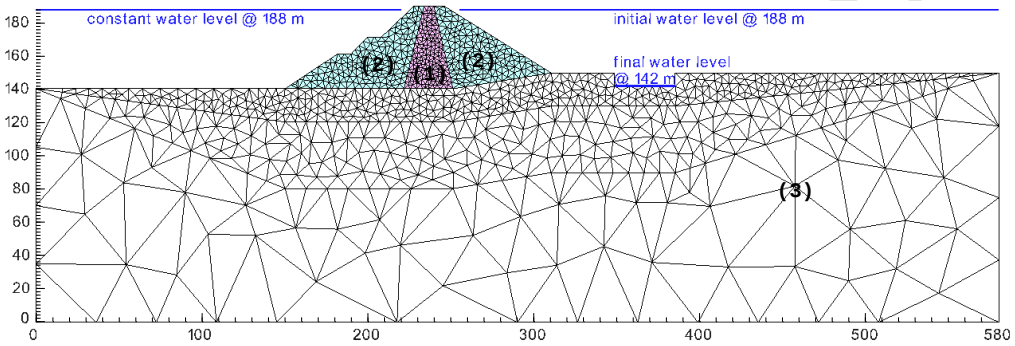

Figure 17: Example 3: Embankment dam. Geometry and mesh. The water level at the right-hand side is slowly lowered. No ponding is allowed. Mesh with 6-node triangles and 3 integration points.

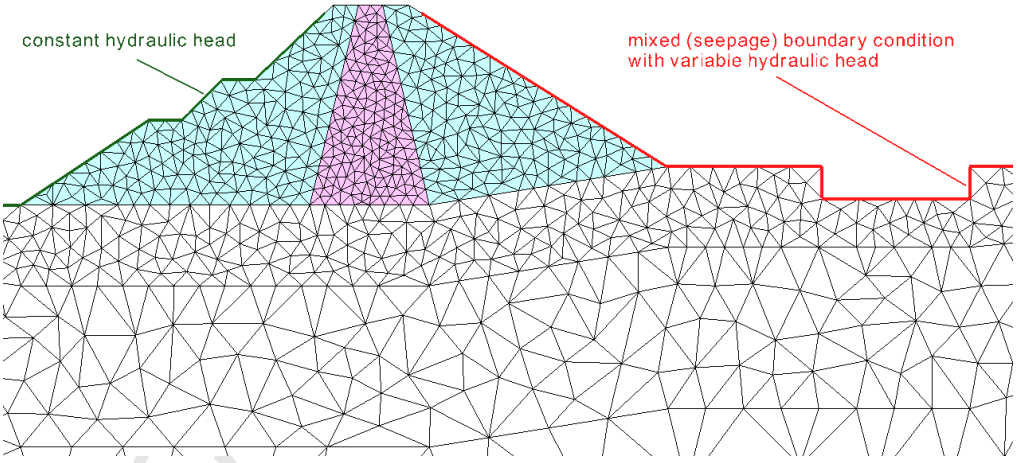

Figure 18: Example 3: Embankment dam. Boundary conditions (all other boundaries are impermeable).

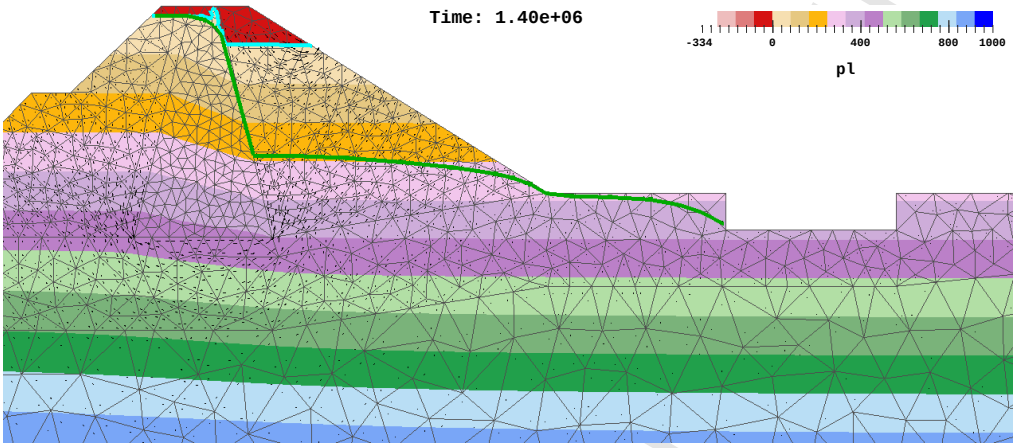

Figure 19: Example 3: Embankment dam at $t = 1.4 \cdot 10^6$. The calculated phreatic line is shown in light blue. The reference line is shown in green with square markers [9]. Arrows indicate the partial relative velocity ($\times 500000$).

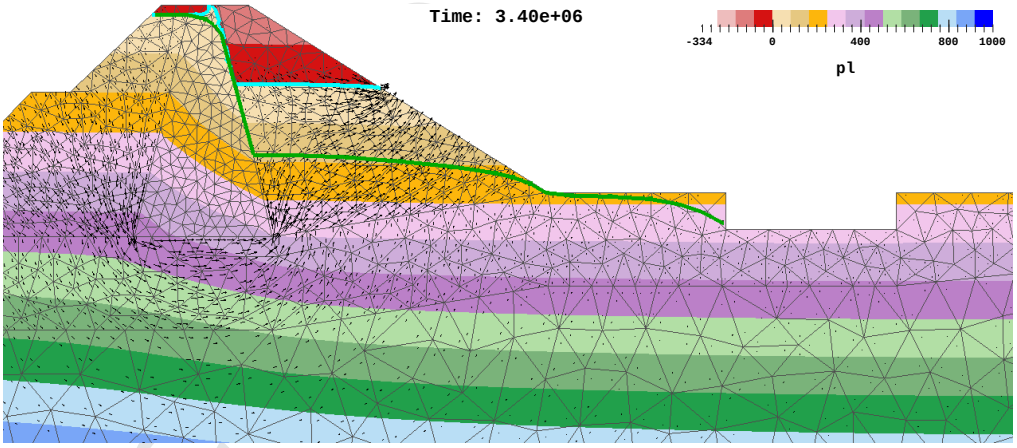

Figure 20: Example 3: Embankment dam at $t = 3.4 \cdot 10^6$. The calculated phreatic line is shown in light blue. The reference line is shown in green with square markers [9]. Arrows indicate the partial relative velocity ($\times 500000$).

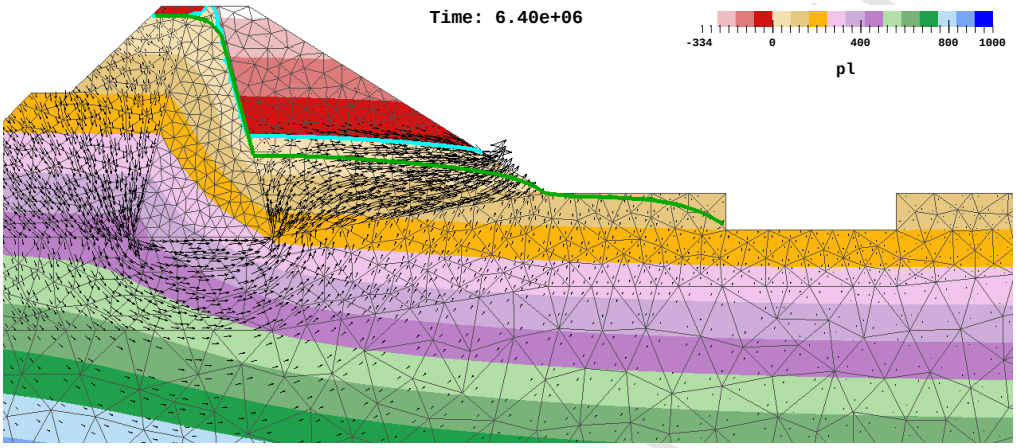

Figure 21: Example 3: Embankment dam at $t = 6.4 \cdot 10^6$. The calculated phreatic line is shown in light blue. The reference line is shown in green with square markers [9]. Arrows indicate the partial relative velocity ($\times 500000$).

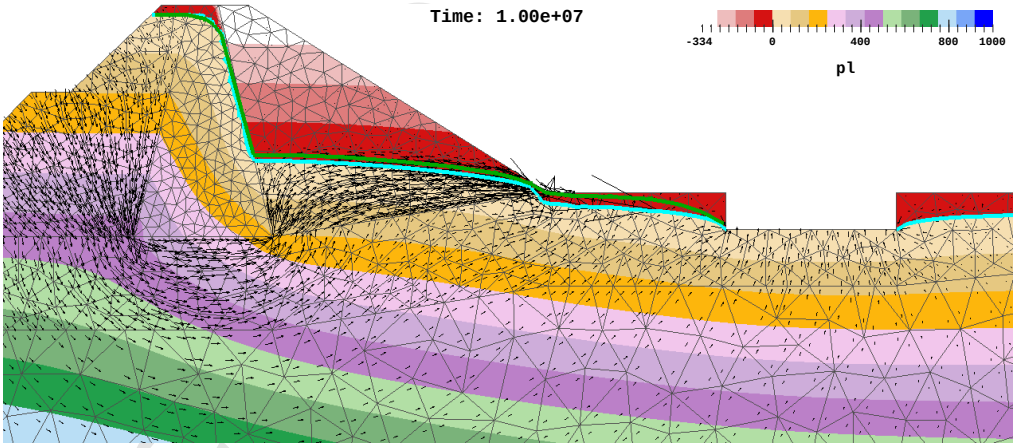

Figure 22: Example 3: Embankment dam at $t = 10^7$. The calculated phreatic line is shown in light blue. The reference line is shown in green with square markers [9]. Arrows indicate the partial relative velocity ($\times 500000$).

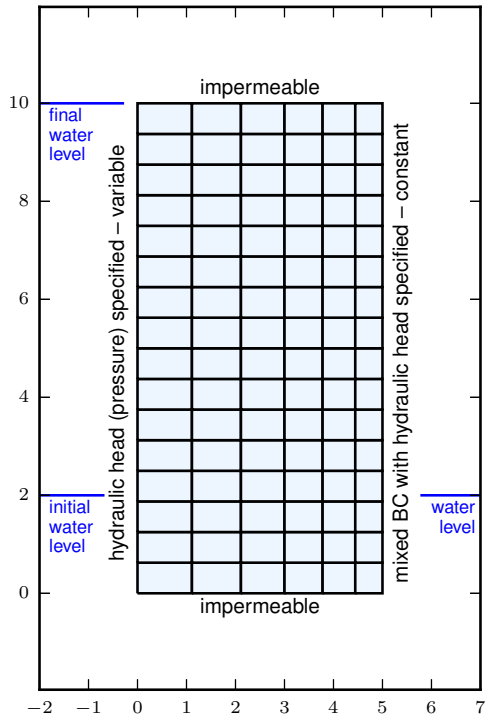

Figure 23: Example 4: Wetting of rectangular domain. Geometry, mesh and boundary conditions. Mesh with 8-node quadrilaterals and 9 integration points.

Therefore, if the purpose is solely to find the steady state (phreatic line), either approach can be employed but the drainage simulation of Example 1 is usually faster in terms of computing time.

5.5. Example 5: Rectangular porous domain with infiltration

This example employs the same geometry of Example 1 and additionally simulates a quick infiltration process due to wetting (Fig. 25). After a simulation (stage 1) is carried out as in Example 1 and the results from the final unsaturated state are saved, another simulation (stage 2) is carried out starting with the saved pressure-saturation state and by applying a flux to the upper and right hand sides with $\bar{q}_\ell$ varying from $\bar{q}_\ell = 0$ to $\bar{q}_\ell = -0.5$, linearly from $t = 0$ to $t = 100$ with $\Delta t = 0.1$. The results from stage 2 are illustrated in Fig. 26 where we can see the infiltration at the top with a change of flow direction and increase of liquid saturation.

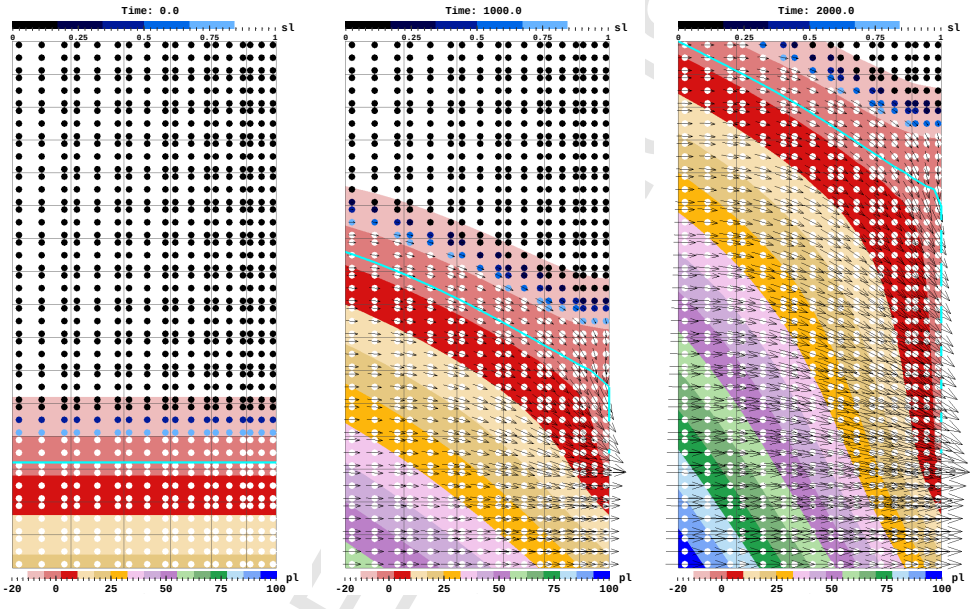

(a) (b) (c)

Figure 24: Example 4: Wetting of unsaturated rectangular domain. Dots indicate saturation values. Arrows indicate partial relative velocity ($\times 0.5$). (a) $t = 0$. (b) $t = 1000$. (c) $t = 2000$.

A detailed analysis is presented next. The resulting pressure distribution along the right-hand edge is illustrated in Fig. 27 for the two stages. The corresponding liquid retention behaviour is shown in Fig. 28. It can be seen that at the end of the drainage process, the final condition exhibits an outflow flux at the seepage face with zero pressure; note the isoline corresponding to $t = 1000$ in Fig. 27a where the pressure from 2 m to approximately 7 m is zero. Upon infiltration, the pressure above 7 m also goes to zero up to near the maximum height (Fig. 27b).

The time variation of saturation and relative velocity are illustrated in Figs. 29 and 30, respectively. At the end of the infiltration process, the right-most edge is completely saturated with zero pressure almost everywhere above 2 m. In Fig. 30a, we observe that the vertical relative velocities at the integration points of elements (a), (b), (c) and (d) reach a maximum magnitude followed by a decrease on magnitude towards a constant value. The increase of magnitude coincides with the approaching phreatic line which causes the velocity vector to rotate clockwise (pointing downwards) since flow cannot cross the unsaturated face. As the phreatic line continues moving downwards, these integration points become more unsaturated reducing the partial relative velocity. Finally, in Fig. 30b, we observe that, after overcoming the unsaturated state, the liquid flow becomes faster due to the infiltration process but reaches a steady flow state towards the end.

5.6. Example 6: Pond in 3D with infiltration

A final example is presented with a three-dimensional simulation of seepage flow and infiltration through an unsaturated embankment dam. As in Example 5, two stages are considered: one for obtaining the steady unsaturated flow and another for infiltration due to rain. The plan view of the example is given in Fig. 31. Due to symmetry, one fourth of the domain is modelled. In addition, the pore pressure is assumed constant from the inside to the middle of the embankment (line indicated by "cut" in Fig. 31). The mesh, geometry and boundary conditions are illustrated in Fig. 32.

The first stage keeps the hydraulic head constant at the two inner vertical faces and lowers the hydraulic head at the two outer sloped faces down to $z = 0$ with seepage/mixed boundary conditions. The simulation (stage 1) is similar to Example 5 and is run from $t = 0$ to $t = 1000$ with $\Delta t = 1$. The resulting free surface is illustrated in Fig. 33a. The second stage keeps the hydraulic head at the two central faces constant and, similarly to Example 5,

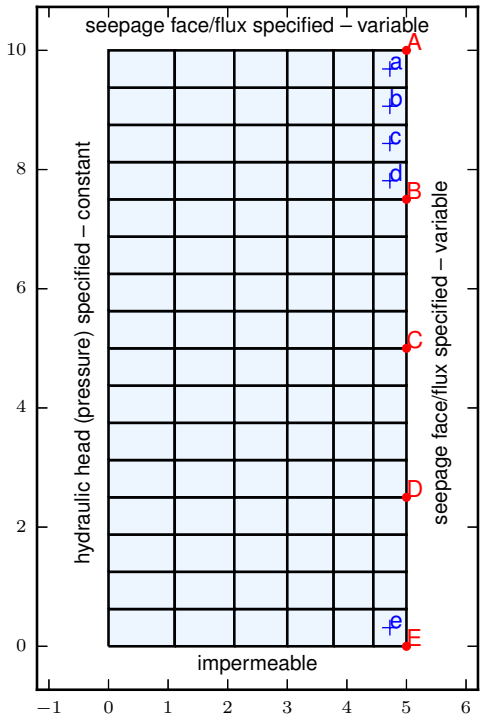

Figure 25: Example 5: Rectangular porous domain with infiltration. Geometry, mesh and boundary conditions. Mesh with 8-node quadrilaterals and 9 integration points. Alphabetical labels indicate selected nodes and elements for data analysis.

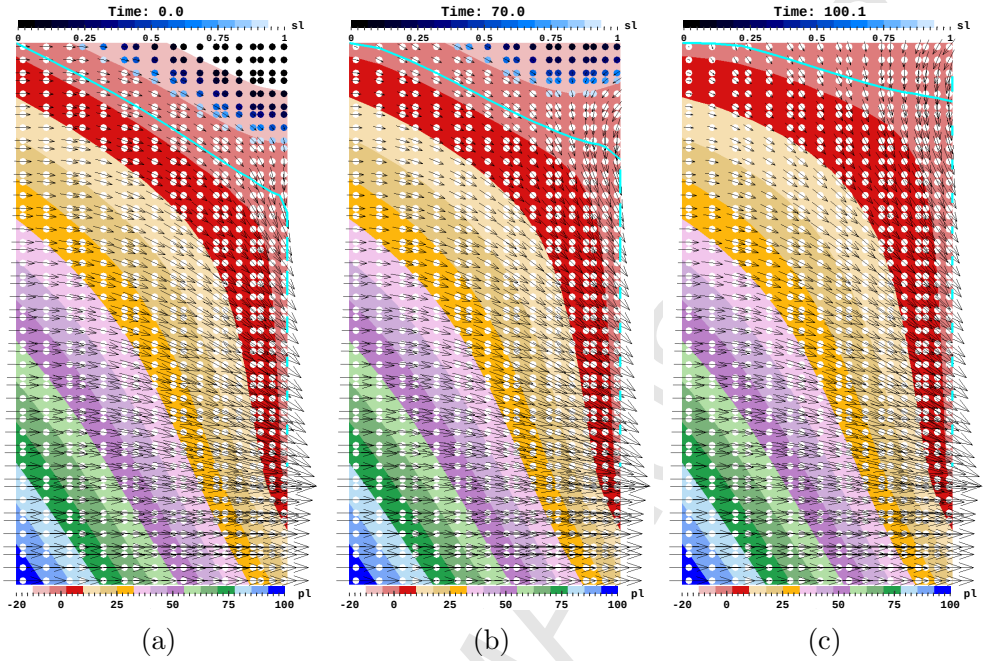

Figure 26: Example 5: Rectangular domain with infiltration. Results from stage 2. Dots indicate saturation. Arrows indicate partial relative velocity ($\times 0.5$). (a) $t = 0$. (b) $t = 70$. (c) $t = 100$.

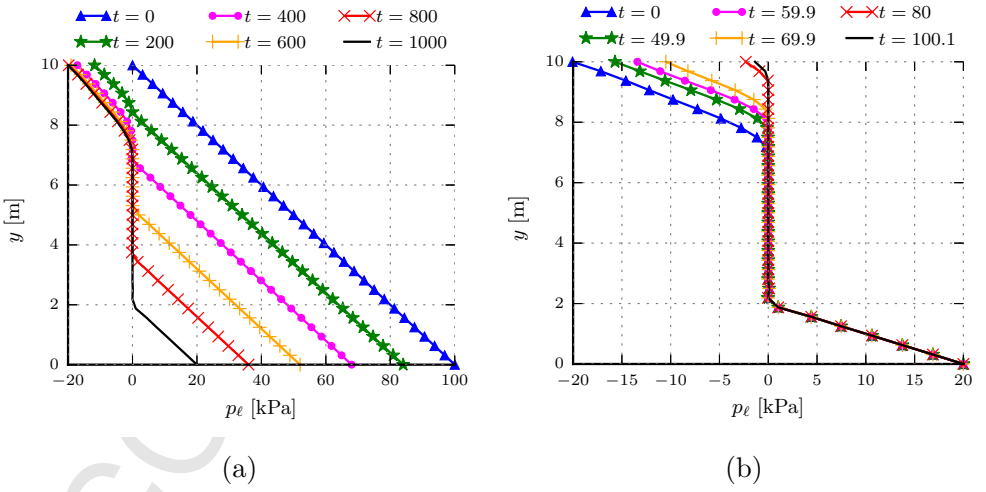

Figure 27: Example 5: Rectangular domain with infiltration. Pressure distribution along the right-most edge. (a) during lowering of liquid level. (b) during infiltration.

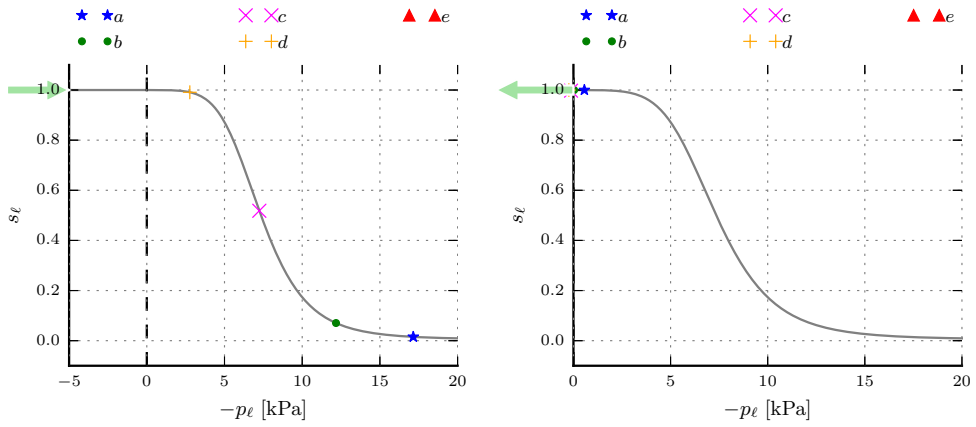

(a) (b)

Figure 28: Example 5: Rectangular domain with infiltration. Liquid retention behaviour near the right-most edge (selected elements). (a) end of lowering of liquid level. (b) end of infiltration.

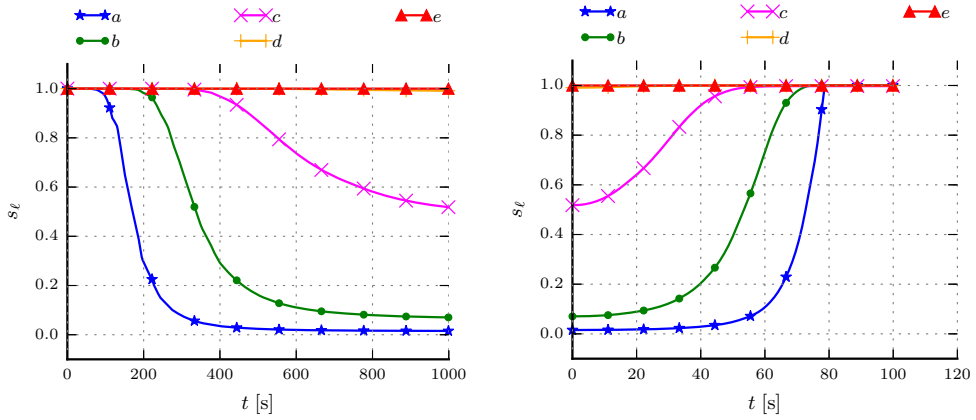

(a) (b)

Figure 29: Example 5: Rectangular domain with infiltration. Saturation evolution near the right-most edge (selected elements). (a) during lowering of liquid level. (b) during infiltration.

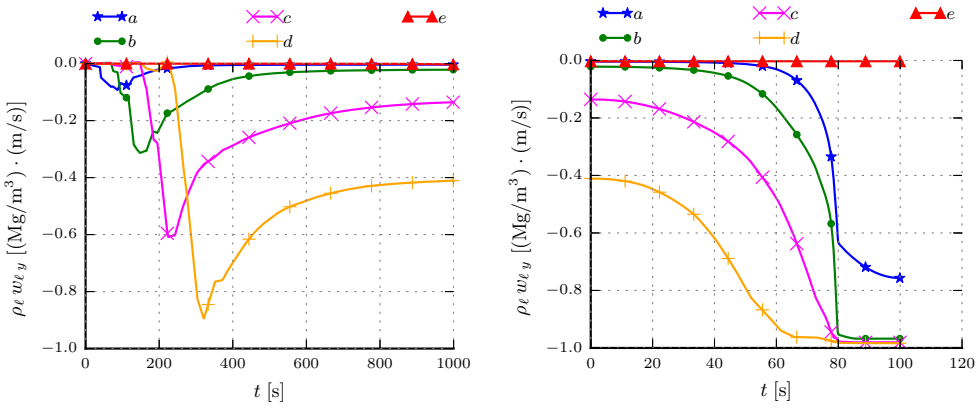

(a) (b)

Figure 30: Example 5: Rectangular domain with infiltration. Partial liquid relative velocity (selected elements) (a) during lowering of liquid level. (b) during infiltration.

applies a linearly increasing (magnitude) flux from $\bar{q}_\ell = 0$ to $\bar{q}_\ell = -1.65$ from $t = 0$ to $t = 100$ with $\Delta t = 0.1$. The resulting free surface is illustrated in Fig. 33b. It can be seen that the model performs quite well and the evolution of the free surface is captured.

Figs. 34 and Fig. 35 present the final liquid pressure distributions for both stages and Fig. 36 presents the partial relative velocity $\rho_\ell \boldsymbol{w}_\ell$ field. During drainage, the velocity vectors on the upper face are horizontal and have larger magnitude towards the centre (saturated region). On the other hand, at the end of infiltration, the direction of flow changes to the inside of the domain due to the applied flux; see arrows pointing to the interior of the embankment in Fig. 36b.

The results at selected nodes and integration points of finite elements are presented in Figs. 37, 38 and 39 and are somewhat similar to the results from Example 5. The de-saturation process is observed in stage 1 with the pressure along the highlighted edge becoming negative (Fig. 37a) and the elements (a), (b), (c) and (d) becoming unsaturated (Fig. 38a). The partial relative velocity at these elements increase and decrease upon the movement of the free surface (Fig. 39a). During the infiltration process (stage 2), the pressure becomes more positive (Fig. 37b), some elements more saturated (Fig. 38b) and the relative velocity varies as illustrated Fig. 39b.

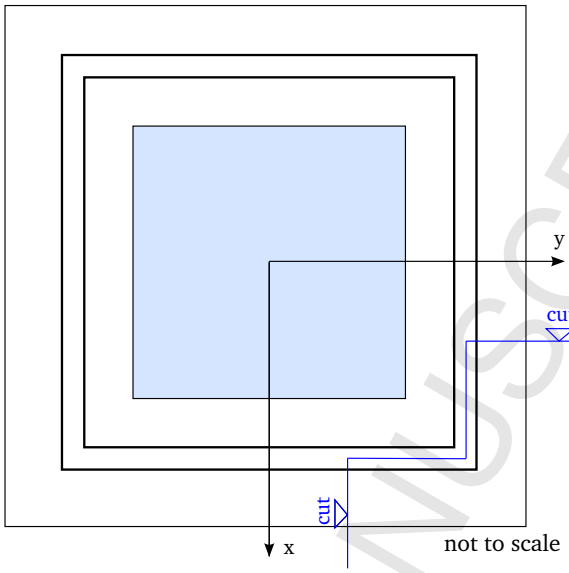

Figure 31: Example 6: Pond in 3D. Top view.

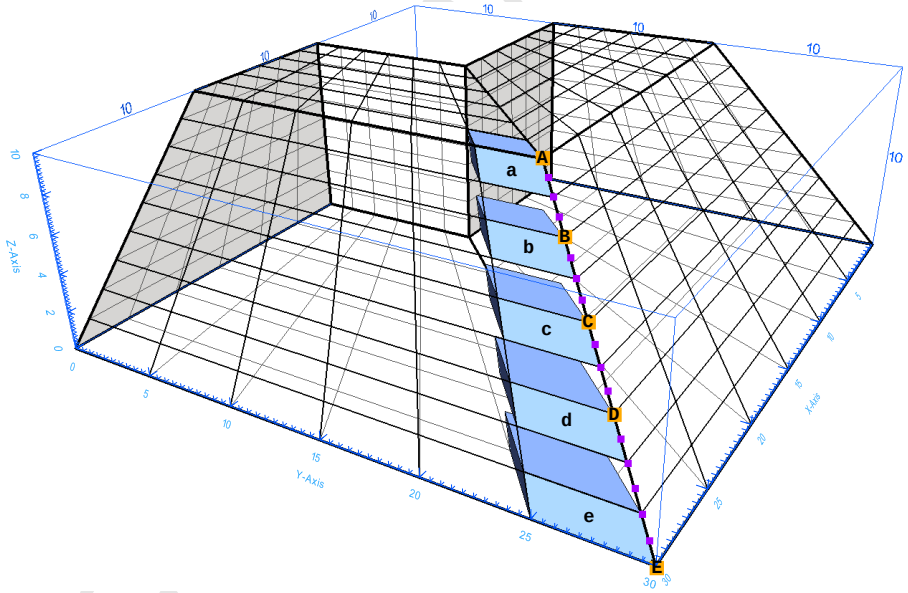

Figure 32: Example 6: Pond in 3D. Geometry, mesh and boundary conditions. Hydraulic head is specified at the two central vertical faces. The two outer sloped faces are set with prescribed (mixed) seepage conditions. All other faces are impermeable. Nodes and elements for analyses are highlighted and labelled with alphabetical tags. Mesh of 20-node hexahedral elements with 27 integration points.

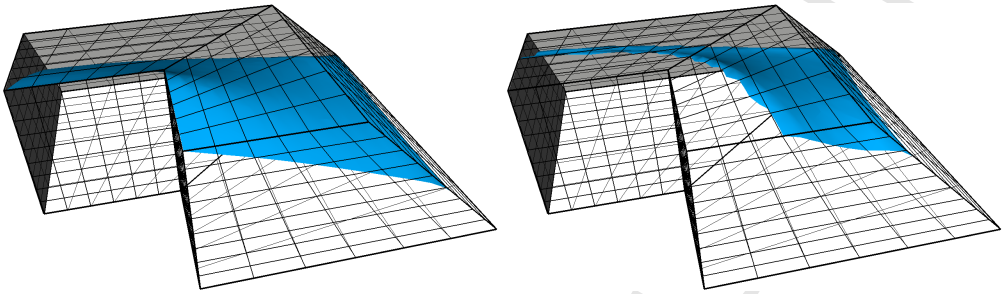

(a) (b)

Figure 33: Example 6: Pond in 3D with infiltration. Free surface approximation with $p_\ell = -0.1$. (a) end of lowering external water level. (b) end of infiltration.

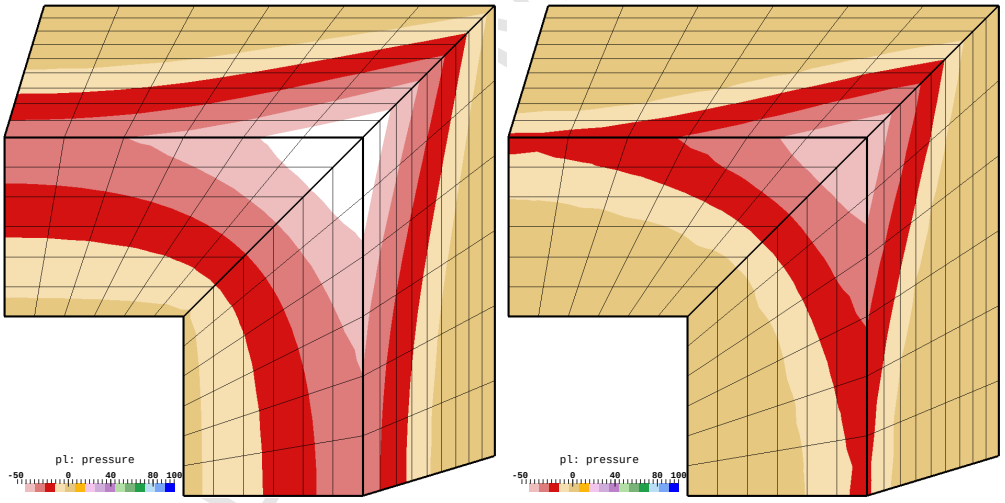

(a) (b)

Figure 34: Example 6: Pond in 3D with infiltration. Pressure distribution. (a) end of lowering external water level. (b) end of infiltration.

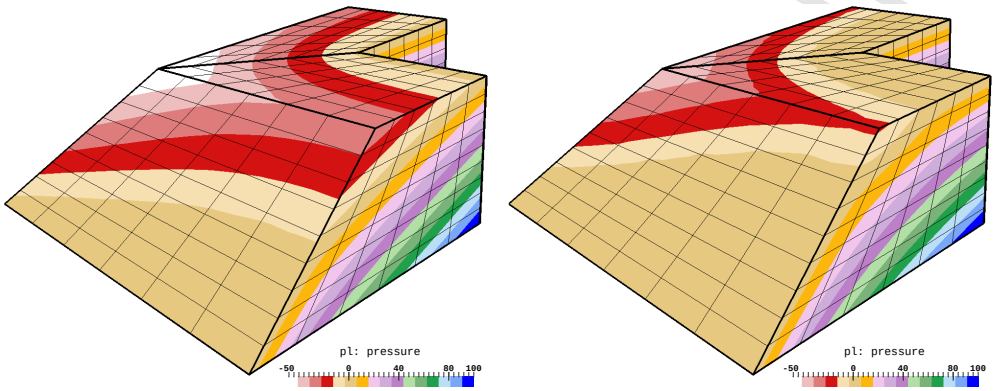

(a) (b)

Figure 35: Example 6: Pond in 3D with infiltration. Pressure distribution. (a) end of lowering external water level. (b) end of infiltration.

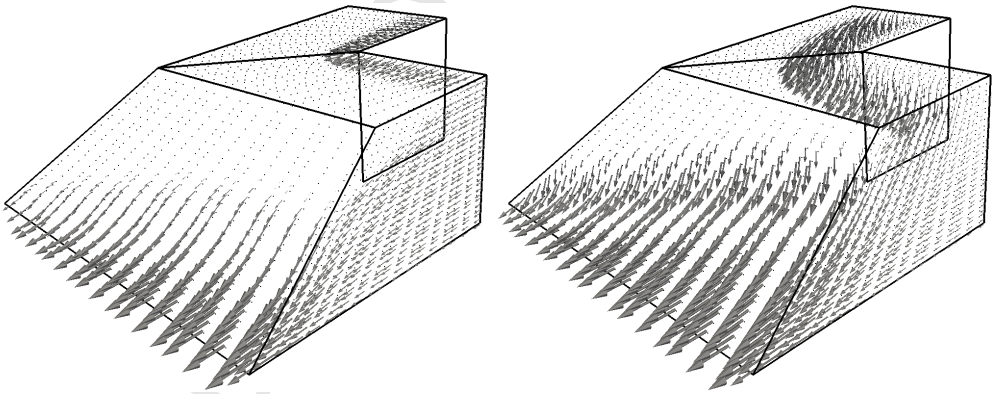

(a) (b)

Figure 36: Example 6: Pond in 3D with infiltration. Partial relative velocity. (a) end of lowering external water level. (b) end of infiltration.

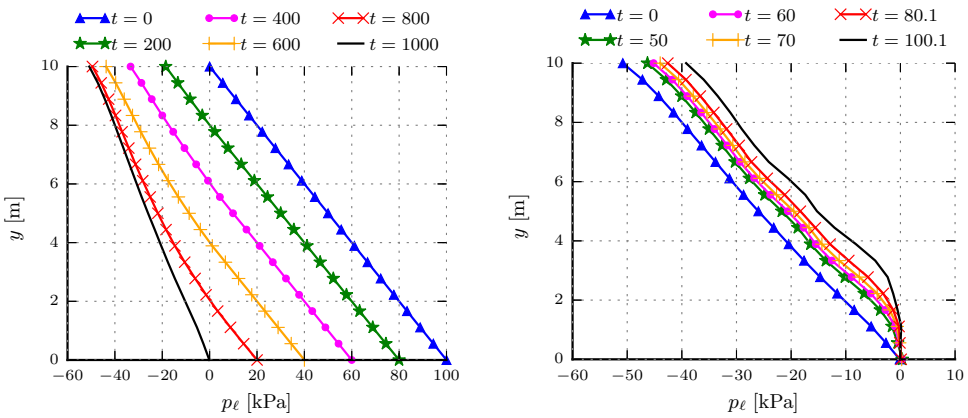

(a) (b)

Figure 37: Example 6: Pond in 3D with infiltration. Pressure distribution along the highlighted edge. (a) during dessication. (b) during infiltration.

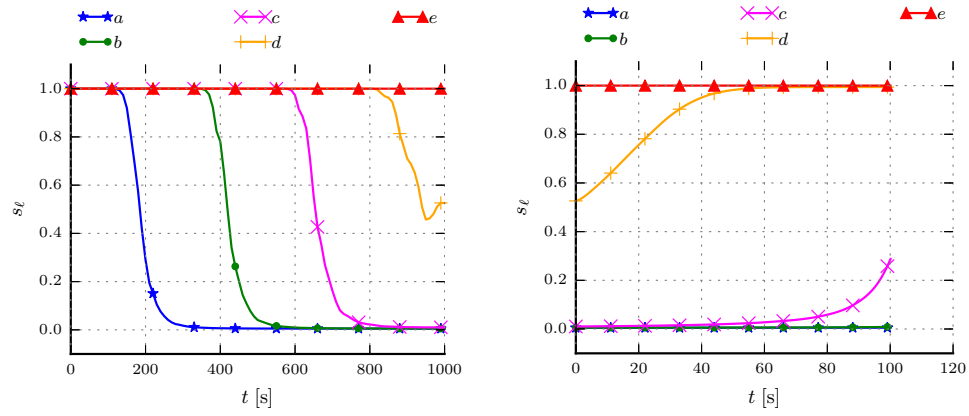

(a) (b)

Figure 38: Example 6: Pond in 3D with infiltration. Liquid saturation. (a) during dessication. (b) during infiltration.

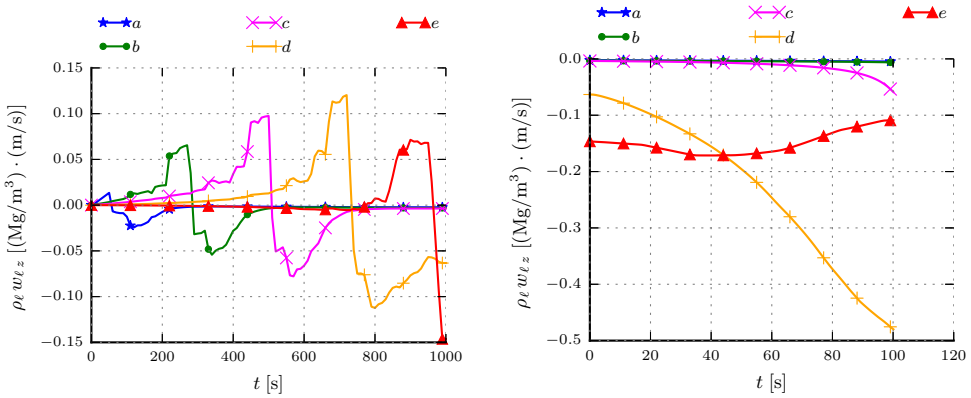

(a) (b)

Figure 39: Example 6: Pond in 3D with infiltration. Partial relative velocity. (a) during dessication. (b) during infiltration.

6. Conclusions

This paper presented a solution to time-dependent seepage including a method to model the unilateral constraints that appear when simulating seepage in partially liquid saturated porous media. The full transient process including the smooth transition from saturated to unsaturated state, and *vice-versa*, is considered. The corresponding governing equations are rationally deduced from the theory of porous media.

The equations are solved with the finite element method in which a new degree of freedom (DOF) is introduced. This DOF enriches the finite element where a seepage face is expected and allows for the complete definition of specified pressure (ponding), infiltration rate, seepage face with outward flow, or simply an impermeable face boundary condition. The set of added DOFs require additional equations rendering the global system similar to a solution with Lagrange multipliers. Nonetheless, the unilateral constraint (seepage face) is modelled via a local discretisation.

Careful attention is also given to the modelling of partial density at the surface of the element since it depends not only on the intrinsic density, but also on the liquid saturation and pressure. An extrapolation technique is employed to solve (approximate) this problem.

A fully implicit formulation is derived; therefore the solver using Newton's method is expected to be robust and quadratically convergent.

A number of verification examples are presented demonstrating the accuracy of the proposed method by means of comparisons with other numerical results obtained for the specific situation of steady state. Some examples involving drainage and infiltration are also given in order to further illustrate the predictive capabilities of the formulation. For instance, the three-dimensional free surface and its time-dependent evolution can be directly modelled.

Appendix A. Derivatives for Jacobian matrix

Derivative of $C_{p\ell}$:

$$\frac{\mathrm{d}C_{p\ell}}{\mathrm{d}p_\ell} = n_f \left(\rho^\ell \frac{\mathrm{d}C_c}{\mathrm{d}p_c} - 2\, C_c\, C_\ell \right) \tag{A.1}$$

Derivatives related to R_ℓ^m:

$$\frac{\mathrm{d}\bar{r}_\ell}{\mathrm{d}p_\ell^n} = S^n \left[\frac{\mathrm{d}C_{p\ell}}{\mathrm{d}p_\ell} (\beta_1\, p_\ell - \psi_\ell^*) + \beta_1\, C_{p\ell} \right] \tag{A.2}$$

$$\frac{\mathrm{d}(\rho_\ell\, \dot{\boldsymbol{w}}_\ell)}{\mathrm{d}p_\ell^n} = \ddot{\boldsymbol{K}}_\ell^{sat} \cdot \left[S^n \frac{\mathrm{d}k_\ell^r}{\mathrm{d}p_\ell} \left(\rho^\ell\, \dot{\boldsymbol{g}} - \nabla\, p_\ell \right) + k_\ell^r \left(S^n\, C_\ell\, \dot{\boldsymbol{g}} - \dot{\boldsymbol{G}}^n \right) \right] \tag{A.3}$$

$$\frac{\mathrm{d}r_x}{\mathrm{d}p_\ell^n} = S^n\, \rho_\ell\, \kappa\, \bar{H}(f_\ell + \kappa\, g) + \langle\langle f_\ell + \kappa\, g \rangle\rangle \frac{\mathrm{d}\rho_\ell}{\mathrm{d}p_\ell^n} \tag{A.4}$$

$$\frac{\mathrm{d}r_x}{\mathrm{d}f_\ell^n} = S^n\, \rho_\ell\, \bar{H}(f_\ell + \kappa\, g) \tag{A.5}$$

Derivatives related to R_f^μ:

$$\frac{\mathrm{d}r_f}{\mathrm{d}p_\ell^n} = -S^n\, \bar{H}(f_\ell + \kappa\, g) \tag{A.6}$$

$$\frac{\mathrm{d}r_f}{\mathrm{d}f_\ell^n} = S^n \left[1 - \bar{H}(f_\ell + \kappa\, g) \right] \tag{A.7}$$

Derivative of the ramp function resulting in the Heaviside function:

$$\frac{\mathrm{d}\langle x \rangle}{\mathrm{d}x} \equiv H(x) = \begin{cases} 0 & \text{if } x < 0 \\ 1 & \text{if } x > 0 \\ 1/2 & \text{otherwise} \end{cases} \tag{A.8}$$

Derivative of the smooth ramp function:

$$\frac{\mathrm{d}\langle\langle x \rangle\rangle}{\mathrm{d}x} \equiv \bar{H}(x) = \frac{1}{1 + \exp\left(-\beta\, x\right)} \tag{A.9}$$

Acknowledgements

The support of the Australian Research Council (ARC) under grant DE120100163 is gratefully acknowledged. The anonymous reviewers are also acknowledged for their critical review.

References

[1] J. Oden, N. Kikuchi, Theory of variational inequalities with applications to problems of flow through porous media, International Journal of Engineering Science 18 (1980) 1173–284. doi:10.1016/0020-7225(80)90111-1.

[2] M. Harr, Groundwater and seepage, Dover, 1991.

[3] T. J. R. Hughes, The finite element method: linear static and dynamic finite element analysis, Dover Civil and Mechanical Engineering Series, Dover Publications, 2000.

[4] K.-J. Bathe, M. R. Khoshgoftaar, Finite element free surface seepage analysis without mesh iteration, International Journal for Numerical and Analytical Methods in Geomechanics 3 (1979) 13–22. doi:10.1002/nag.1610030103.

[5] S. J. Lacy, J. H. Prevost, Flow through porous media: A procedure for locating the free surface, International Journal for Numerical and Analytical Methods in Geomechanics 11 (1987) 585–601. doi:10.1002/nag.1610110605.

[6] R. I. Borja, S. S. Kishnani, On the solution of elliptic free-boundary problems via newton's method, Computer Methods in Applied Mechanics and Engineering 88 (1991) 341–61. doi:10.1016/0045-7825(91)90094-M.

[7] M. Budhu, D. Contractor, C. S. Wu, Modelling groundwater changes due to fluctuating dam discharge, Applied Mathematical Modelling 18 (1994) 665–71. doi:10.1016/0307-904X(94)90391-3.

[8] J.-P. Bardet, T. Tobita, A practical method for solving free-surface seepage problems, Computers and Geotechnics 29 (2002) 451–75. doi:10.1016/S0266-352X(02)00003-4.

[9] H. Zheng, D. F. Liu, C. F. Lee, L. G. Tham, A new formulation of Signorini's type for seepage problems with free surfaces, International Journal for Numerical Methods in Engineering 64 (2005) 1–16. doi:10.1002/nme.1345.

[10] C. Callari, A. Abati, Finite element methods for unsaturated porous solids and their application to dam engineering problems, Computers & Structures 87 (2009) 485 – 501. doi:10.1016/j.compstruc.2008.12.012.

[11] H. Zheng, H. C. Dai, D. F. Liu, A variational inequality formulation for unconfined seepage problems in porous media, Applied Mathematical Modelling 33 (2009) 437 –50. doi:10.1016/j.apm.2007.11.012.

[12] M. J. Kazemzadeh-Parsi, F. Daneshmand, Unconfined seepage analysis in earth dams using smoothed fixed grid finite element method, International Journal for Numerical and Analytical Methods in Geomechanics 36 (2012) 780–97. doi:10.1002/nag.1029.

[13] R. de Boer, Theory of Porous Media: Highlights in Historical Development and Current State, Springer Berlin Heidelberg, 2000. doi:10.1007/978-3-642-59637-7.

[14] W. Ehlers, Foundations of multiphasic and porous materials, in: W. Ehlers, J. Bluhm (Eds.), Porous Media: Theory, Experiments and Numerical Applications, Springer Berlin Heidelberg, 2002, pp. 3–86. doi:10.1007/978-3-662-04999-0_1.

[15] D. Sheng, S. W. Sloan, A. Gens, D. W. Smith, Finite element formulation and algorithms for unsaturated soils. Part I: Theory, International Journal for Numerical and Analytical Methods in Geomechanics 27 (2003) 745–65. doi:10.1002/nag.295.

[16] D. Sheng, D. W. Smith, S. W. Sloan, A. Gens, Finite element formulation and algorithms for unsaturated soils. Part II: Verification and application, International Journal for Numerical and Analytical Methods in Geomechanics 27 (2003) 767–90. doi:10.1002/nag.296.

[17] D. Sheng, S. W. Sloan, A. Gens, A constitutive model for unsaturated soils: thermomechanical and computational aspects, Computational Mechanics 33 (2004) 453–65. doi:10.1007/s00466-003-0545-x.

[18] D. Sheng, D. G. Fredlund, A. Gens, A new modelling approach for unsaturated soils using independent stress variables, Canadian Geotechnical Journal 45 (2008) 511–34. doi:10.1139/T07-112.

[19] D. M. Pedroso, D. J. Williams, A novel approach for modelling soil-water characteristic curves with hysteresis, Computers and Geotechnics 37 (2010) 374–80. doi:10.1016/j.compgeo.2009.12.004.

[20] D. M. Pedroso, D. J. Williams, Automatic calibration of soil–water characteristic curves using genetic algorithms, Computers and Geotechnics 38 (2011) 330–40. doi:10.1016/j.compgeo.2010.12.004.

[21] D. Sheng, Review of fundamental principles in modelling unsaturated soil behaviour, Computers and Geotechnics 38 (2011) 757–76. doi:10.1016/j.compgeo.2011.05.002.

[22] D. M. Pedroso, A consistent u-p formulation for porous media with hysteresis, International Journal for Numerical Methods in Engineering (2014) 1–29. doi:10.1002/nme.4808.

[23] O. Zienkiewicz, R. Taylor, J. Zhu, The Finite Element Method: Its Basis & Fundamentals, Elsevier, 2005.

[24] K. Bathe, Finite Element Procedures, Prentice Hall, 2006.

[25] R. W. Lewis, B. A. Schrefler, The Finite Element Method in the Static and Dynamic Deformation and Consolidation of Porous Media, 2nd Edition, Wiley, 1998.

[26] R. Durand, M. M. Farias, A local extrapolation method for finite elements, Advances in Engineering Software 67 (2014) 1–9. doi:10.1016/j.advengsoft.2013.07.002.

[27] A. Abati, Models and finite element methods for porous media subjected to localized strains, Ph.D. thesis, Department of Civil Engineering, University of Rome "*Tor Vergata*", 2008.

[28] E. A. de Souza Neto, D. Perić, D. R. J. Owen, Computational Methods for Plasticity: Theory and Applications, John Wiley & Sons, 2008. doi:10.1002/9780470694626.

[29] P. M. A. Areias, T. Rabczuk, Smooth finite strain plasticity with non-local pressure support, International Journal for Numerical Methods in Engineering 81 (2010) 106–34. doi:10.1002/nme.2686.

[30] D. M. Pedroso, D. Sheng, J. Zhao, The concept of reference curves for constitutive modelling in soil mechanics, Computers and Geotechnics 36 (2009) 149–65. doi:10.1016/j.compgeo.2008.01.009.